Spring 5-17-2019

Computation of Flow Fields due to Single- and Twin-Jet Impingement

Xiang Zhang
Washington University in St. Louis

WASHINGTON UNIVERSITY IN ST. LOUIS

James McKelvey School of Engineering
Department of Mechanical Engineering and Material Science

Thesis Examination Committee:
Ramesh Agarwal, Chair
David Peters
Swami Karunamoorthy

Computation of Flow Fields due to Single- and Twin-Jet Impingement

by

Xiang Zhang

A dissertation presented to the James McKelvey School of Engineering

of Washington University in St. Louis

in partial fulfillment of the requirements for the degree of

Master of Science

May 2019
St. Louis, Missouri

Table of Contents

List of Figures

Nomenclature

C_p= Pressure coefficient

D = diameter of water jet pipe

H = vertical distance from exit of pipe to impingement plane

S = Distance between the centerlines of two jets

Re = Reynolds number based on the diameter of pipe

R_{Re} = ratio of Reynolds numbers

y^+= dimensionless wall distance of first grid layer

P = static pressure

P_{ref} = reference pressure produced by gravity

ρ = density of water

V_{inlet} = velocity at jet inlet

V_b = average velocity near exit of jet

V_{max} = maximum velocity

Acknowledgments

I would like to specially thank my research advisor, Dr. Agarwal, for his professional guidance, enthusiastic encouragement and helpful critiques on my research work.

I want to thank Dr. Peters and Dr. Karunamoorthy for serving on the committee.

I would also like to thank my parents for their love and support on whatever I pursue.

I am grateful to all my friends in the CFD lab. Thanks to their help and suggestions that helped me a lot in my work.

ABSTRACT OF THIS THESIS

Computation of Flow Fields due to Single- and Twin-Jet Impingement

By

Xiang Zhang

Master of Science in Mechanical Engineering

Washington University in St. Louis, 2019

Research Advisor: Professor Ramesh K. Agarwal

The thesis consists of two parts. The first part focuses on numerical simulations and their comparison with experimental data for single-jet impingement on ground. Angles between the axisymmetric jet and impingement surface considered are 15, 30 and 90 degree. It is shown that both the k-epsilon and Wray-Agarwal (WA) model can predict the flow fields in good agreement with the experimental results. The second part extends the first part to twin-jet normal impingement on the ground. It focuses on numerical simulation of fountains formed by the twin-jet impingement. The fountains can be normal straight upward when the two jets are identical and can become inclined or even curved when the two jets are of different velocities and/or diameters. For jets' exits close to the impingement surface, some important flow phenomenon of fountains are studied for various inlet jet Reynolds numbers, impingement heights above the ground and distance between the twin jets. The incompressible Reynolds-Averaged Navier-Stokes (RANS) equations with k-epsilon and WA turbulence model are solved using the commercial CFD solver Ansys Fluent for computation of the flow fields

Chapter 1: Numerical Simulation of Single-jet Impingement on Ground at Various Angles

1.1 Introduction

There have been many investigations on impinging jet flow fields due to their significance in many engineering applications. For example, impinging jets are used in cooling system of high-pressure turbine blades that face extremely high temperatures in gas turbine engines [1-4]. Impingement flow is very complex and the flow field is highly dependent on impingement height H (height from jet exit to impingement plane), Reynolds number and shape of the jet nozzle and impingement angle.

Wang et al. [5] conducted an experiment on jet impingement flow fields at different impingement angles and Reynolds numbers. Ghaneeizad et al. [6] performed experiments on a submerged water jet impinging on a flat surface under confined conditions and cohesive sediment erosion parameters were studied. Shademan et al. [7] conducted CFD analysis of impinging jets at different impingement heights using a variety of turbulence models. Greco et al. [8] investigated flow features in the near field of single and twin synthetic jets to evaluate the influence of distance between the centerline of the jets of 1.1, 3 and 5 nozzle diameters on interaction between the jets.

In the impinging jet experiment conducted by Wang et al. [4], some of the data points are asymmetric and not sufficient enough because of their limited number. The goal of this study is to conduct CFD simulations of impinging jet flow fields and compare

the CFD simulations with experimental results; the validated CFD results can then be used to calculate many flow fields by varying various impinging jet parameters namely the jet height above the ground, jet diameter and Reynolds number to obtain a thorough understanding of the flow fields for wide range of parameters which is difficult to obtain experimentally.

In the CFD study, incompressible RANS equations are solved with realizable k-epsilon model and one-equation Wray-Agarwal model on a solution independent properly refined structured grid. Numerical method is validated with the experimental data and then minor differences between the numerical and experimental results are discussed and explained.

1.2 Numerical Method and Validation

1.2.1 Physical Model and Grid

The computational domain is a cuboid with the same size as the experimental apparatus of Wang et al. [5]. The length*width*height of the domain is 5000mm*300mm*400mm as shown in Figure 1.1. Other parameters of physical model are kept the same as in the experiment; the diameter of pipe is 20mm and height from the exit of pipe to the impingement plane is 3D = 60mm. Figure 1.1 (b) shows the schematic of the flow field due to a normal round submerged water jet impinging on a flat plane illustrating different regions of the jet – the free jet region, the impingement region and wall jet region.

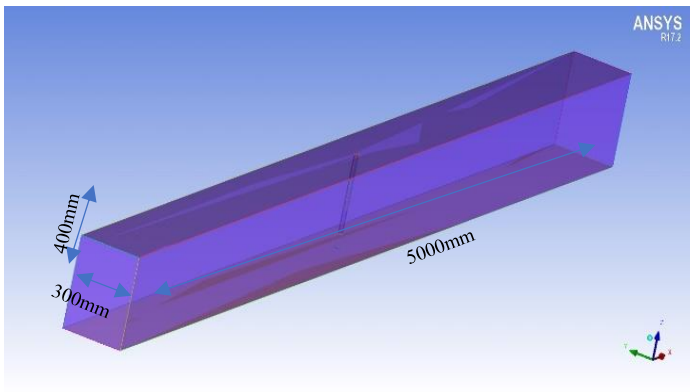

Figure 1.1 (a): Computational domain

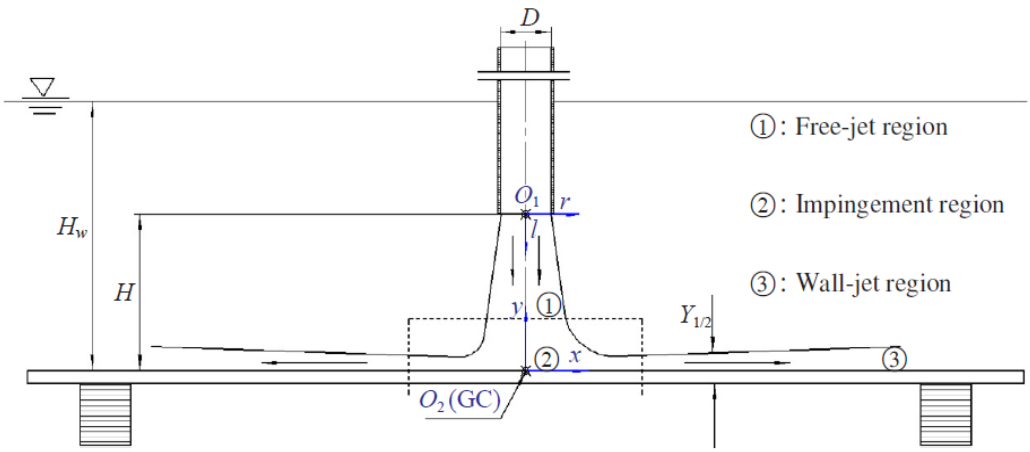

Figure 1.1 (b): Schematic of flow field due to a normal round submerged water jet impinging on a flat plane

A structured grid is used and refined in the boundary layer regions on the impingement plane and in interior surface of pipe as shown in Figure 1.2. The grid size of first layer is 7×10^{-4}m from interior surface of pipe and is 1×10^{-5}m from impingement plane to ensure that y+ < 1 near the wall. Around the pipe, a cuboid block with square cross-section area is created. In this block, three layers of O-grid are used: the first layer of O-grid is associated with the exterior surface of the pipe; the second one is associated with the interior surface of the pipe; grids inside the third

O grid are adapted to the flow in the pipe. Figure 1.2(c) shows that the grid is of very high quality.

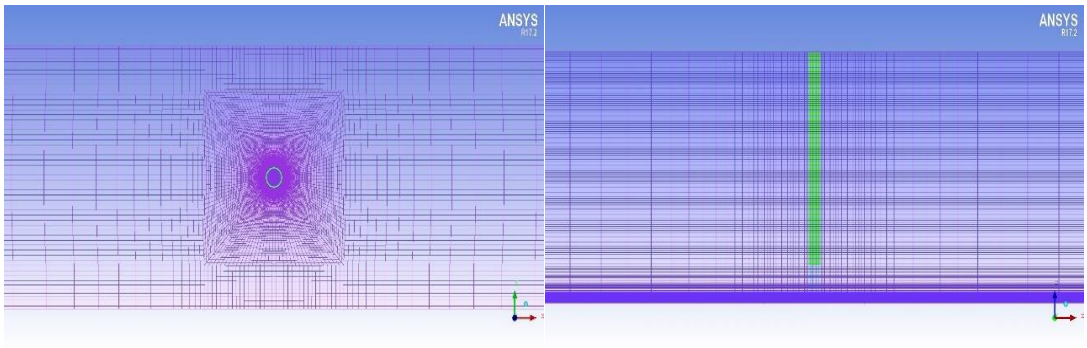

(a) Grid in the jet region in the pipe (b) Grid near the impingement plane

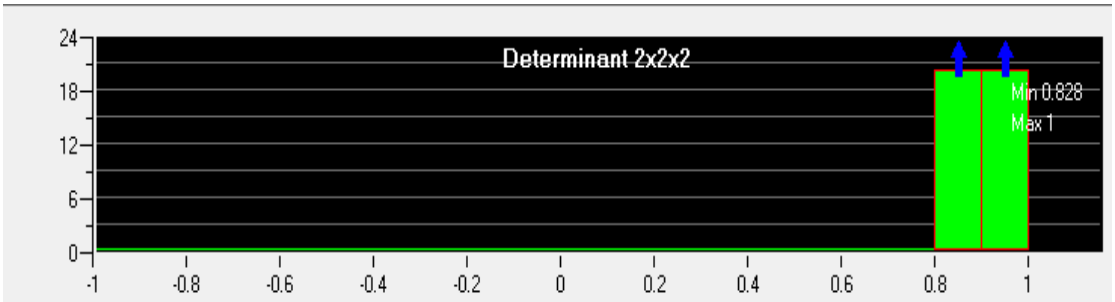

(c): Pre-mesh quality under determinant 2*2*2 criterion

Figure 1.2 Structured mesh and its quality.

1.2.2 Numerical Model

The double precision solver in ANSYS Fluent is used to perform the numerical simulations. Incompressible Reynolds-Averaged Navier-Stokes (RANS) equations with realizable k-epsilon and Wray-Agarwal (WA) turbulence model are solved on the solution independent structured grid. Near wall treatment is kept as 'default' in the solver as standard wall functions near the wall are used with realizable k-epsilon model. WA model does not require any near wall treatment in the low Reynolds

number region. SIMPLE scheme with second order discretization for convection and diffusion terms is selected for the solution algorithm.

The inlet boundary condition at the pipe is set as velocity inlet where the velocity magnitude is 1.17m/s and velocity is normal to fluid surface. The upper surface of cuboid is set as pressure outlet where the gauge pressure is 0. The other surfaces are set as static walls without slip. Gravity acceleration is applied as 9.81m/s^2 and specific density is 0. The material for the entire domain is water whose density is 998.2kg/m3 and viscosity is 0.001003kg/(m • s). The solution is considered converged when the average pressure in the impingement region of the plane and the average velocity along the centerline line below the jet exit at l/D=1.5 does not change more than 0.1% after 1000 iterations.

1.3 Results and Discussion

1.3.1 Initial Condition of the Jet Flow

Figure 1.3 (a) shows the definition of average velocity, vb, and maximum velocity, vm, in the jet flow. In this study, vb and vm are used to normalize the velocity profiles and the diameter of jet D is used to normalize the length parameters, e.g. axial distance l, radial distance r, etc. The average velocity vb in this case is 1.28m/s, corresponding to Re (= vb D/υ, υ is the kinematic viscosity of water = 1*10-6) = 25,600. Figure 1.3(b) shows the velocity profile near the exit of the jet flow (l/D=0.5) from both CFD and experimental results; there is an excellent agreement between the two.

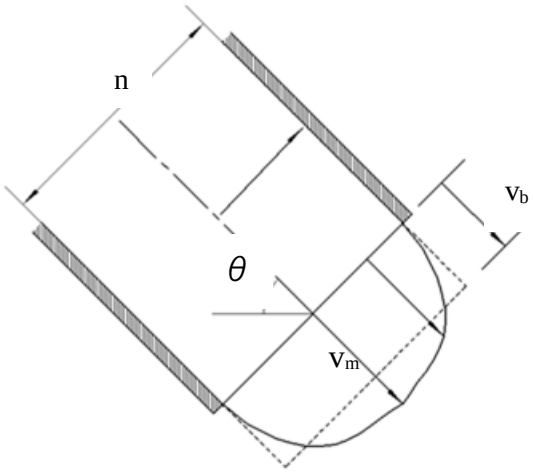

(a) Definitions of average velocity vb and maximum velocity vm in jet flow

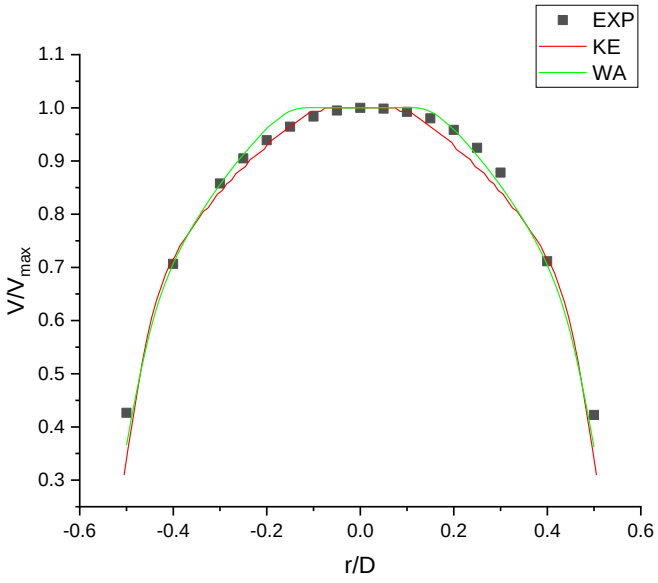

(b): Normalized velocity near exit (l/D=0.5) at θ=90

Figure 1.3 Velocity profile after exit from pipe

1.3.2 Velocity Profiles between Jet Exit and Impingement Plane

Figure 1.4 shows the normalized computed and experimental velocity profiles v/vb at various l/D for normal impingement at Re=25,600 and H/D=3. The magnitude of velocity decreases rapidly as |r/D| becomes greater than 0.5, especially in the region near the impingement plane.

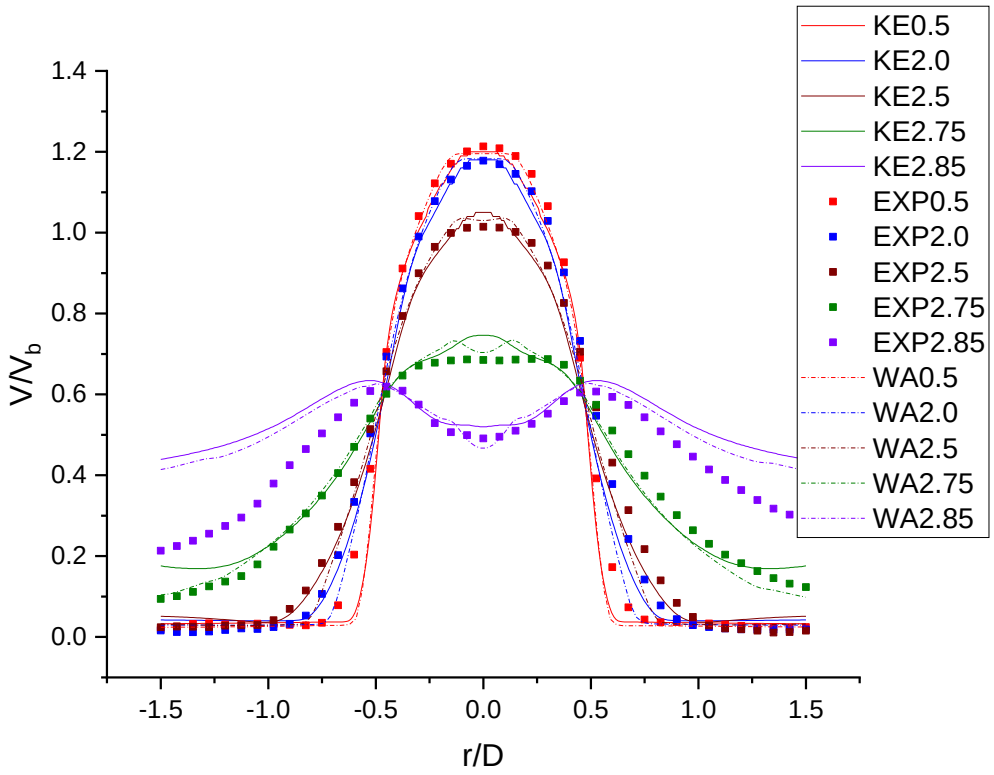

Figure 1.4: Velocity profiles along the centerline after jet exit

Figure 1.5 shows the normalized velocity along the centerline of the jet from jet exit to impingement plane when impingement angle is 90, 30 and 15 degree. The velocity decreases significantly after l/D=2.5 where the flow transitions from free jet region to impingement region. CFD results, both from k-epsilon and WA turbulence model show excellent agreement with experiment results when impingement angle is 90 degree. When impingement is 15 and 30 degree, there are some differences between the CFD and experimental results. A possible reason for this can be that when creating a structured mesh, it is harder to refine the grids in the regions of interest rfor inclined jets than for normal jets.

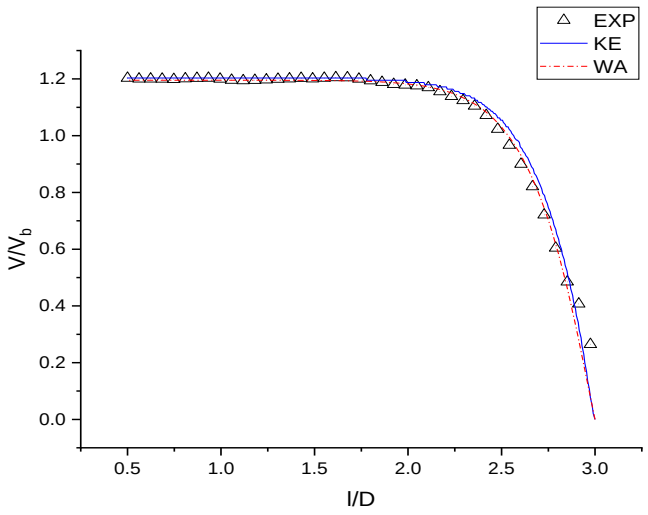

(a) 90 degree

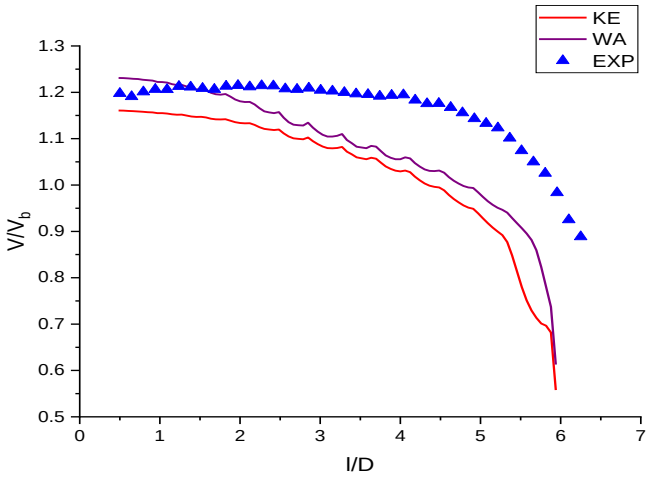

(b) 30 degree

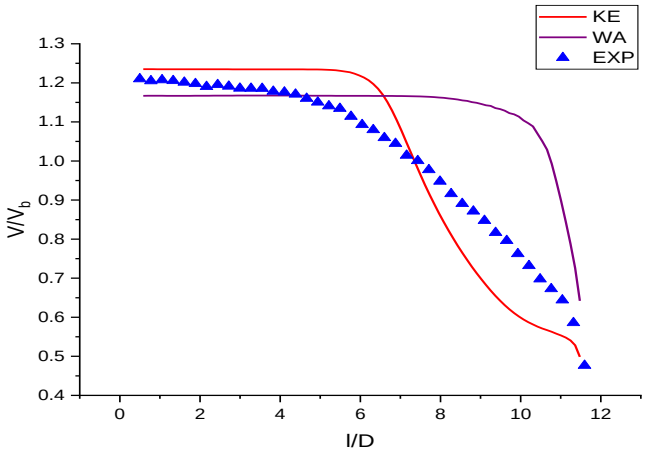

(c) 15 degree

Figure 1.5: Velocity along the jet centerline at different impingement angles.

Figure 1.6 shows the normalized velocity profiles along the centerline of the jet and at different locations parallel to the centerline. The peak velocity occurs where r/D is +/- 0.5 at l/D = 2.91 when v/vb reaches 0.62 approximately. The agreement between the CFD, whether k-epsilon or WA model, and experimental results is overall very good. There is some asymmetry in the experimentally measured velocity profiles in the experiment. As a result, there are small differences in the CFD results and the experimental results on two sides of the centerline.

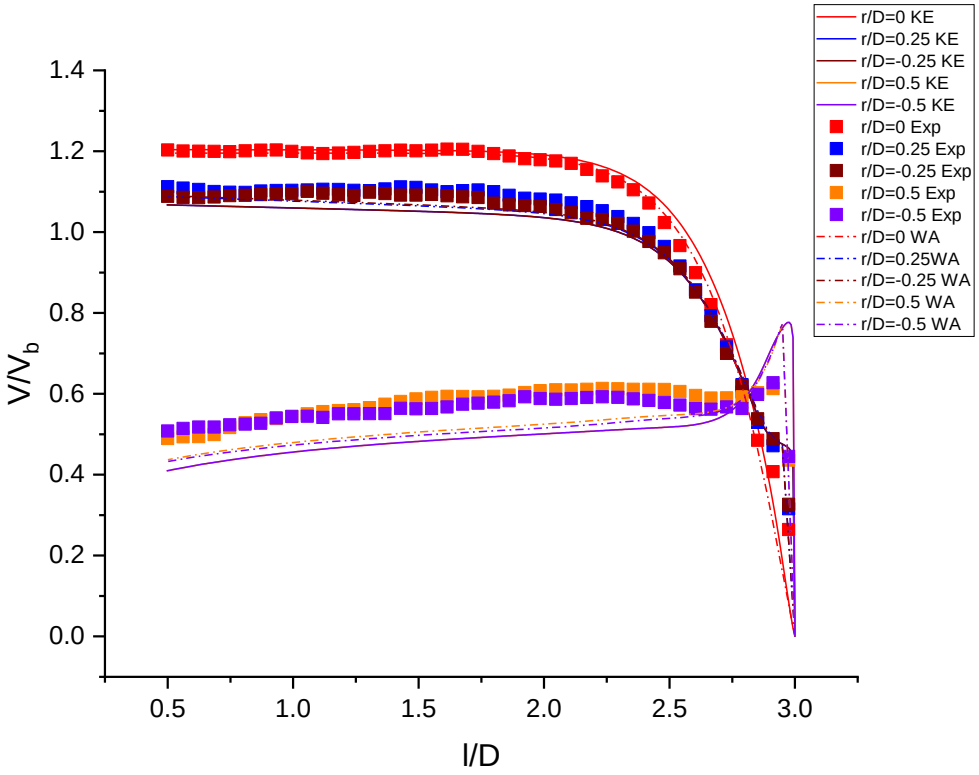

Figure 1.6 Normalized velocities along lines parallel to centerline at different radial distances from jet.

Figure 1.7 shows the normalized maximum velocity in the wall jet region and a series of velocity ratios for different scaling along x-direction in the wall jet region. It can be seen that CFD results match with experimental data best at 90 degree impingement angle.

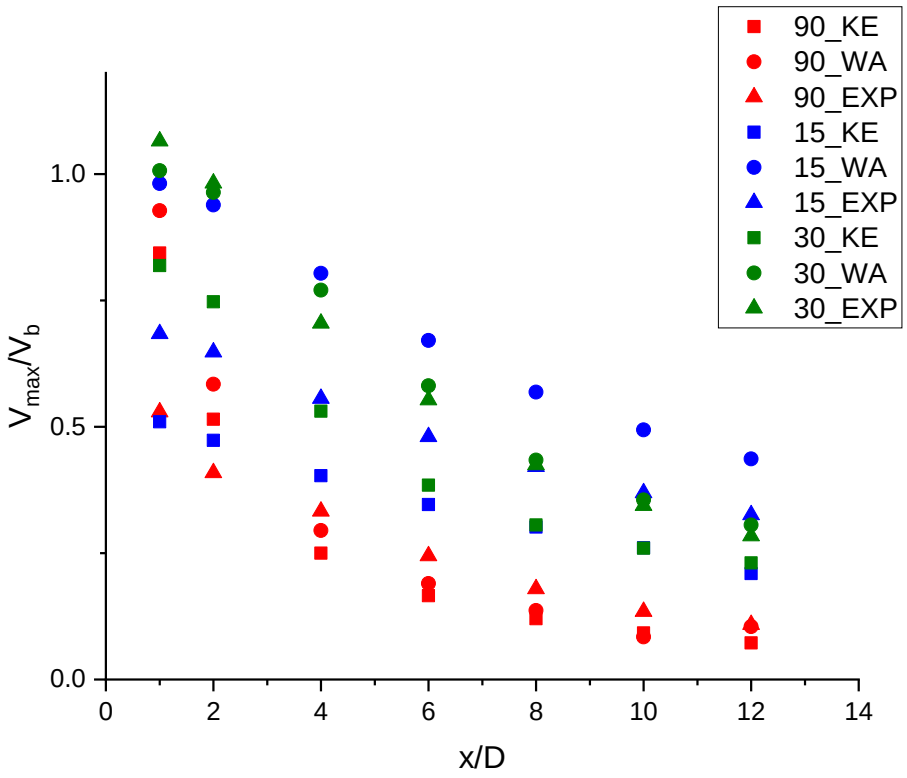

Figure 1.7 Normalized maximum velocity at various radical distances at different impingement angles.

The velocity contours from numerical simulation and experiment are shown in Figure 1.8. The entrainment of surrounding water due to jet is obvious. The stagnation point is located at the centerline of the jet as expected.

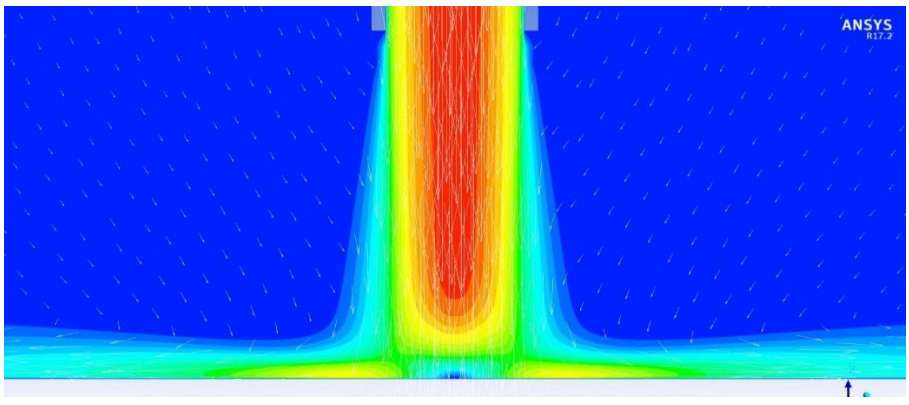

(a) Computed velocity contours

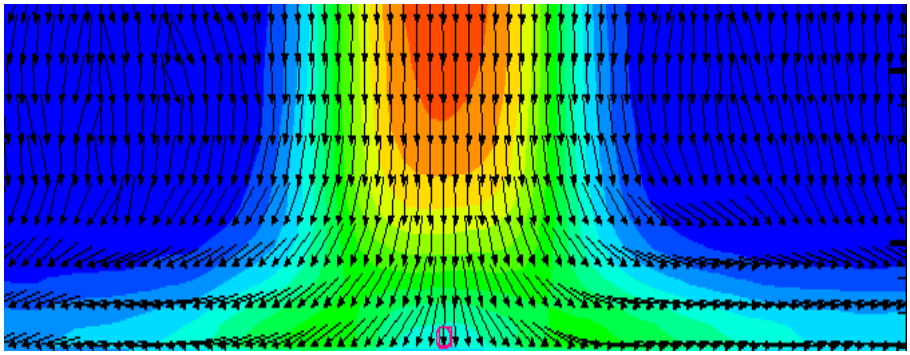

(b) Experimental velocity contours

Figure 1.8 Velocity contours and vectors.

1.3.3 Pressure Coefficient Distribution along Impingement Plate

The pressure coefficient in the impingement plane is defined as $C_p = \frac{P-P_{ref}}{\frac{1}{2}\rho V_b^2}$ where $P_{ref} = \rho gH$. The small difference between CFD result and experiment result could be due to difference in boundary conditions in the experiment and CFD. In the experiment, vb = 1.17m/s is calculated based on velocity measured near the jet exit. In simulation, the boundary condition at velocity inlet was set at 1.17m/s. Due to viscosity of the fluid, velocity at pipe surface is zero. Velocity of jet at centerline gets larger and velocity distribution becomes more uneven as fluid flows through the pipe due to gravity. Figure 1.9 shows the pressure coefficient at different impingement angles. Results from both k-epsilon and WA models show good agreement at 90 degree impingement angle. WA model has better performance at 30 degree while k-epsilon model works better at 15 degree impingement angle.

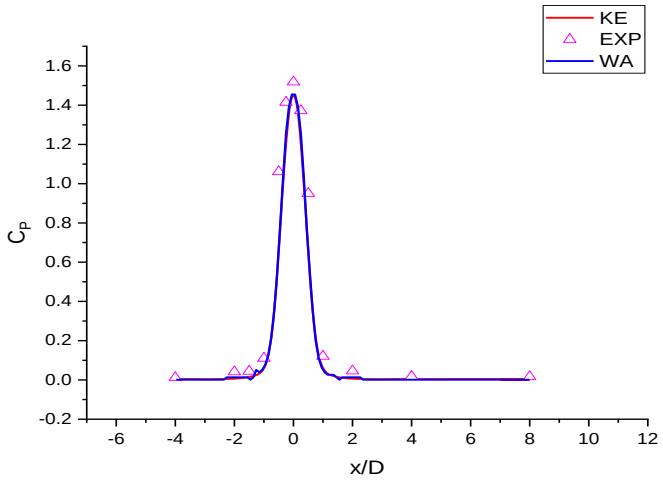

(a) 90 degree

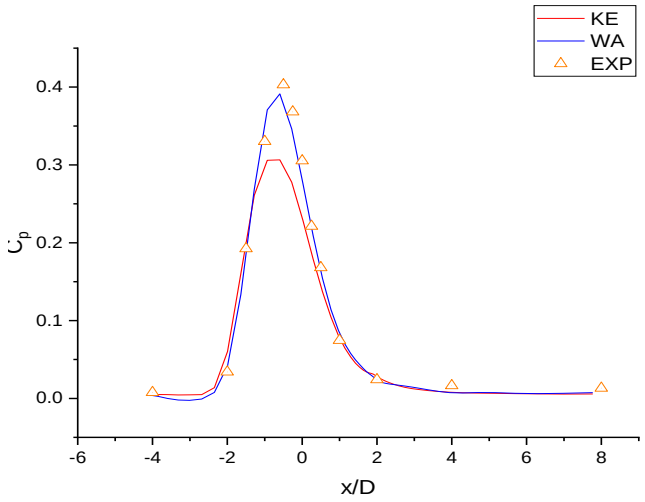

(b) 30 degree

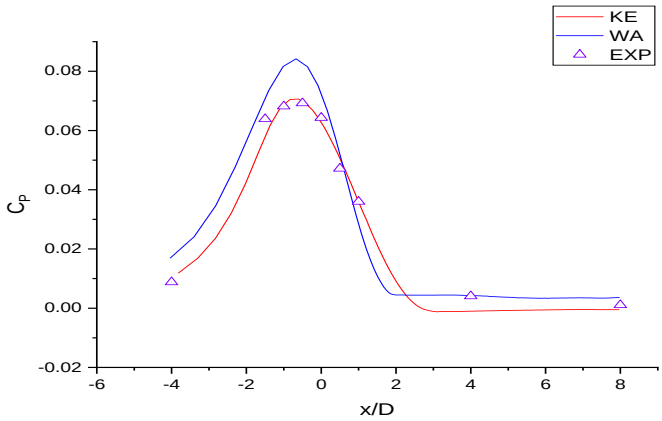

(c) 15 degree

Figure 1.9: Pressure coefficient distribution on ground surface at different impingement angles.

It can be noted from Figure 1.10 that y+ near the impingement region on the plate is less than 1 attesting to the proper implementation of CFD methodology in ANSYS Fluent.

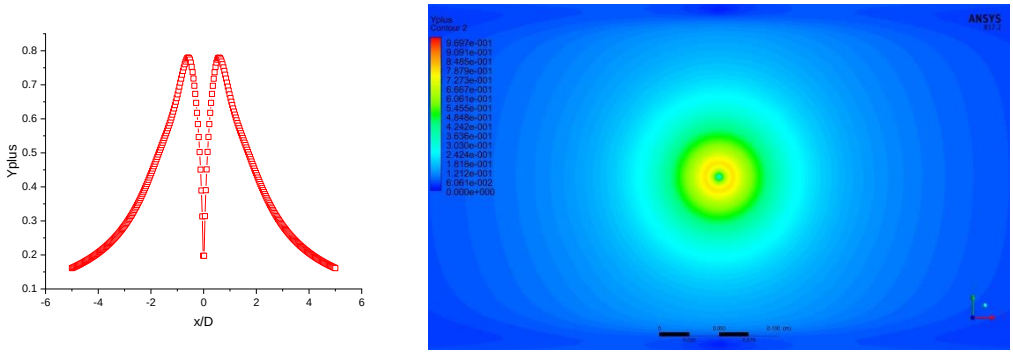

(a) y^+ at different radial distances from stagnation point, (b) in the impingement plane

Figure 1.10 y+ distribution

1.4 Conclusions

Generally, there are always some errors in the numerical simulations even on the finest grid due to order of accuracy of the numerical algorithm, turbulence model and boundary conditions and there is always some uncertainty in the measurements depending upon the measurement technique and other variables in the experimental apparatus. These factors contribute to some mismatch in the CFD and experimental results but overall the agreement between the two in this case is quite good.

Chapter 2: Numerical Simulation of Fountain formed due to Twin-jet Impingement on Ground

2.1 Introduction

Impinging jets have been widely studied because of their significance in many engineering applications. For example, impinging jets are used for industrial cleaning, metal cutting and cooling system of high pressure turbine blades that face extremely high temperatures in gas turbine engine [1, 4, 10]. In another important fighter aircraft application related to the propulsion system of a STOVL or VTOL aircraft, multiple jets from the jet engine can impinge in the close vicinity of the ground during landing and take-off.

Several numerical and experimental studies have been conducted for twin-jet impingement on the ground resulting in fountain formation. Saripalli [11] conducted a flow visualization experiment of twin-jet impingement and studied the basic flow patterns near the stagnation lines and the effect of the ratio of jet momentum on the flow field. Ozmen [12] conducted the experimental investigation of flow characteristics of confined twin air jets at high Reynolds number where downwash fountain was formed. The Reynolds number of the air jet ranged from 30,000 to 50,000, nozzle to plate spacing was in the range 0.5D-4D and the spacing between the jets was in the range 0.5D-2D. Barata et al. [13] measured the velocities in the flow field resulting from single and twin-jet impingement against a wall in the presence of cross-flow by laser-dropper velocimetry. They also performed the RANS

computations using a two-equation turbulence model and compared the computed results against the experimental data. Greco et al. [8] investigated the flow features in the near field region of single and twin synthetic jets to evaluate influence of the jet interactions by varying the distance between the axis of the two jets by 1.1, 3 and 5 times the nozzle diameters. Abdel-Fattah [14] studied the impinging twin-jet flow without cross flow by both the experimental and numerical methods. The parameters in his study considered jet Reynolds number from $9.5*10^4$ to $22.4*10^4$, nozzles to plate spacing of 3D to 12D, nozzle to nozzle spacing of 3D, 5D and 8D, and jet angles from 0 to 20 degrees.

Although several numerical simulations have been reported in the literature, twin-jet impingement has been studied for a very small range of parameters. Also, there is paucity of results for parameters that result in inclined fountain flow in contrast to symmetrical fountain flow. Inclined fountain flow has more engineering importance since impinging jets are difficult to be controlled as completely identical.

In this study, incompressible RANS equations with realizable k-epsilon turbulence model are used to conduct numerical simulations of twin impinging jets. Range of parameters considered include the inlet jet Reynolds number from $2*10^4$ to $8*10^4$, distance between centerlines of twin jets from 1.4D to 16D and ratio of Reynolds number between the two jets from 1 to 4. Velocity and pressure fields are computed and analyzed.

2.2 Numerical Method

2.2.1 Physical Model

The computational domain is a cuboid with length*width*height = 5000mm*1000mm*400mm as shown in Figure 2.1. The physical model is very similar in all cases computed except changes in some parameters. In most cases, D, diameter of the jet, is fixed at 0.02m and impingement height H from jets exit to the ground is fixed at 3D or 6D. The distance between the centerline of jets, S, is changed between various cases.

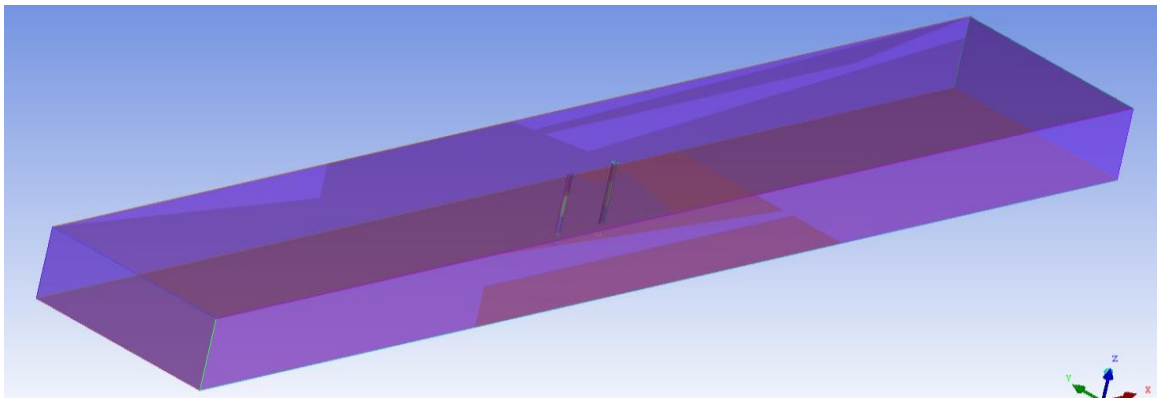

(a) Physical model and 3D computational domain

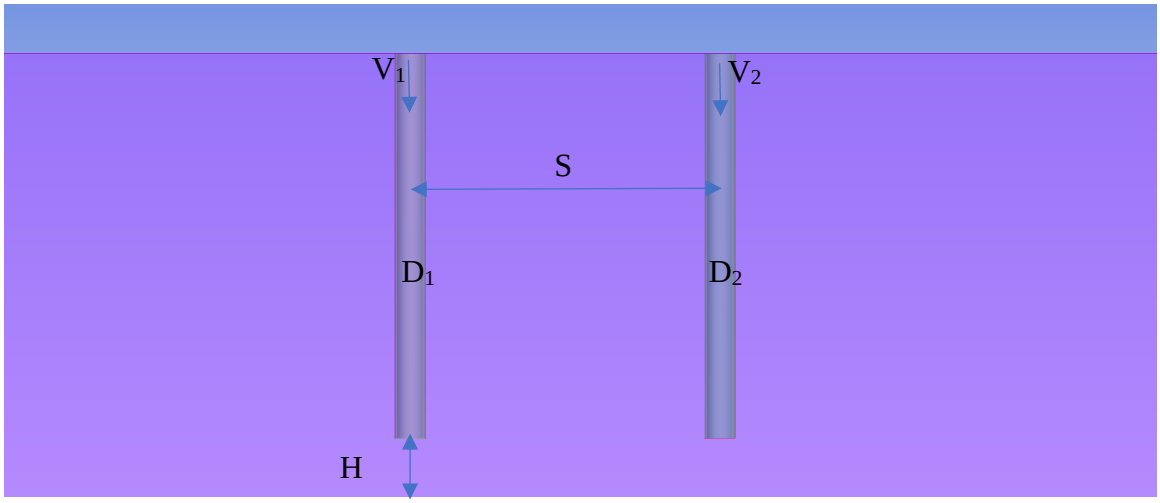

(b) Cross section of physical model

Figure 2.1 Computational domain

Since physical model is not complex, a structured grid is used and refined in regions with large velocity gradients including near the impingement plane, near the interior surface of the pipe from which the jets exit and in the middle of fountain region resulting from twin-jet interaction. The size of first mesh layer is 7×10^{-4}m from interior surface of the pipe and is 1×10^{-5}m from the impingement plane in order to ensure that y+ < 1. Around a pipe, a cuboid block with square cross-section is created. In this block, three layers of O-grid are generated: the edge of first layer of O-grid is associated with exterior surface of the pipe; the second layer of O-grid is associated with interior surface of the pipe; and the grids inside the third O grid are adapted to the flow in the pipe. Figure 2.2 shows the grid refinement regions when the distance between the jets is 16D. Figure 2.3 shows that the grid has good quality under determinant 2*2*2.

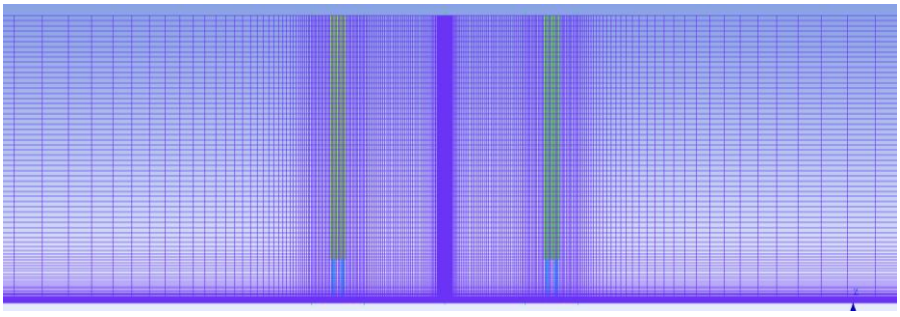

Vertical Cross-section in symmetry plane

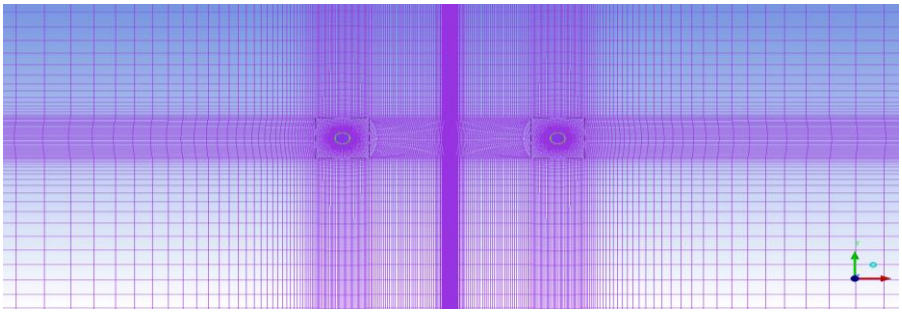

Figure 2.2 Structured grid in the computational domain

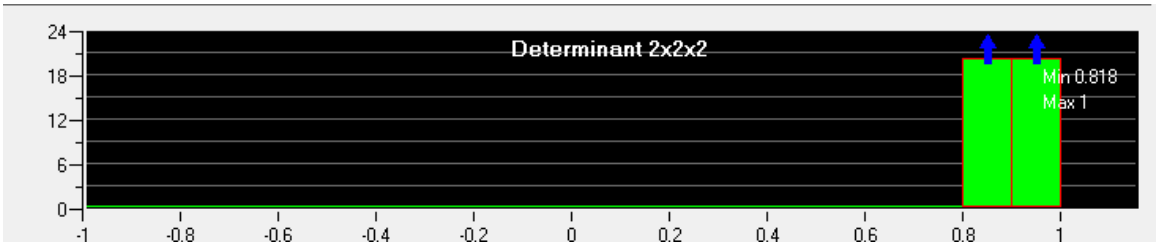

Figure 2.3 Pre-mesh grid quality

2.2.2 Numerical Model

The double precision pressure-based solver in ANSYS Fluent is used to perform the numerical simulations. Incompressible Reynolds-Averaged Navier-Stokes (RANS) equations are solved with realizable k-epsilon turbulence model with standard wall function. SIMPLE algorithm for pressure-velocity coupling and second order accurate method for discretization of convection and diffusion terms are selected.

The inlets of pipes are set as velocity inlets where the velocity is normal to the surface. The upper surface of the cuboid is set as pressure outlet where the gauge pressure is 0. All other surfaces are set as static walls without slip. Gravity acceleration is applied as 9.81m/s^2 and specific density is 0. The material for the entire domain is water whose density is 998.2kg/m^3 and viscosity is 0.001003kg/(m • s). The solution is considered as converged when scaled residuals are lower than 1e-3 and when the average pressure at the bottom of fountain and average velocity above the bottom of the fountain do not change more than 1% after 1000 iterations

2.3 Results and Discussion

2.3.1 Flow Conditions to form a Straight Fountain

When the wall jets produced by jet impingement are of identical strength, they can produce a fountain normal to impingement surface. Therefore, it is critical to find the parameters that form a normal fountain. In this section, the fountain formation is considered by jets of different diameters: $D_1 = 0.02m$ and $D_2 = 0.03m$. To determine the factors that influence the character of the fountain, three cases are conducted. Two cases have twin-jet with different diameters ($D_1 = 0.02m, D_2 = 0.03$m), in which the difference is that in the first case, twin-jets are controlled to have identical mass flow rate while in the second case twin-jets are controlled to have identical Reynolds number. The third case is performed under condition that $D_1 = D_2 = 0.02m$ *and* $V_1 = V_2 = 1.5m/s$. In all three cases, inlet velocity of the left jet is fixed at $V_1 = 1.5m/s$, distance between the two jets is fixed such that S/D = 5 where $D = \sqrt{D_1 * D_2}$. Figures 2.4~2.6 show the velocity contours of the fountain in the three cases. It can be easily observed from Figure 2.4 that when the mass flow rates of two jets of different diameters are the same, the fountain has asymmetry inclining toward the jet of larger diameter; however when the Reynolds numbers of the two jets of different diameter are the same, the fountain formed is straight upward as shown in Figure 2.5 like the reference case when the diameters and velocities of the two jets are same as shown in Figure 2.6. The difference between Figure 2.5 and Figure 2.6 could be due to minor differences in the physical model. Diameter of jet D that is used to create the physical model is $D = \sqrt{D_1 * D_2}$ ($D_1 = 0.02$m, $D_2 =$

0.03m) in Figures 2.4 and 2.5, which is larger than $D = \sqrt{D_1 * D_2}$ ($D_1 = D_2 = 0.02m$) in Figure 2.6. This leads to larger impingement height as well as larger distance between the two jets, which can decrease the strength of fountain when Reynolds number is identical for both cases.

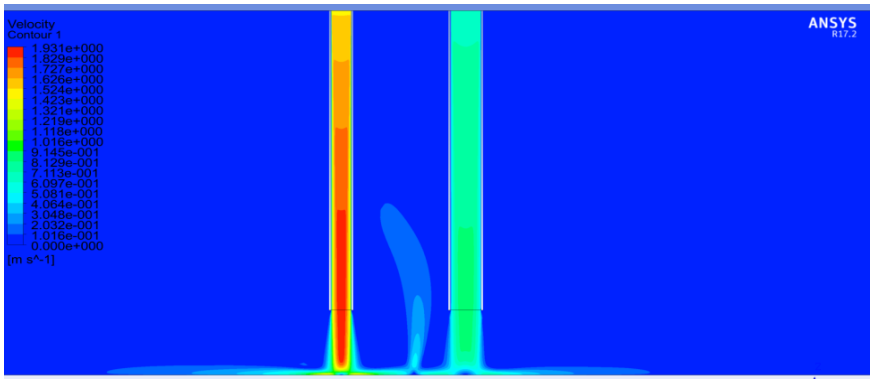

Figure 2.4 Fountain formed by twin jets with identical mass flow rate

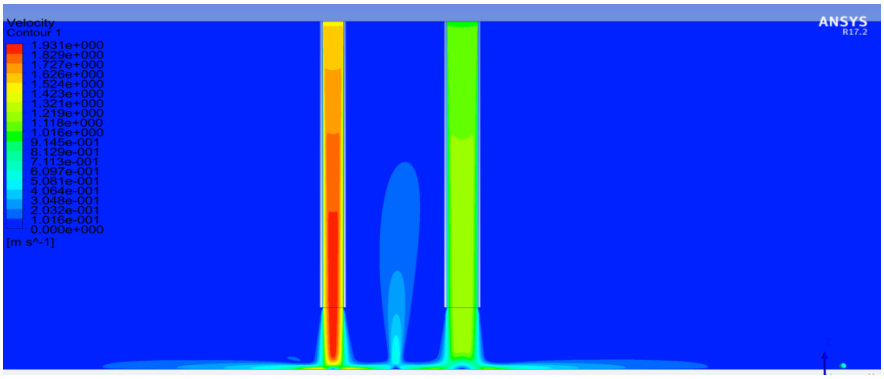

Figure 2.5 Fountain formed by two jets with identical inlet Reynolds number

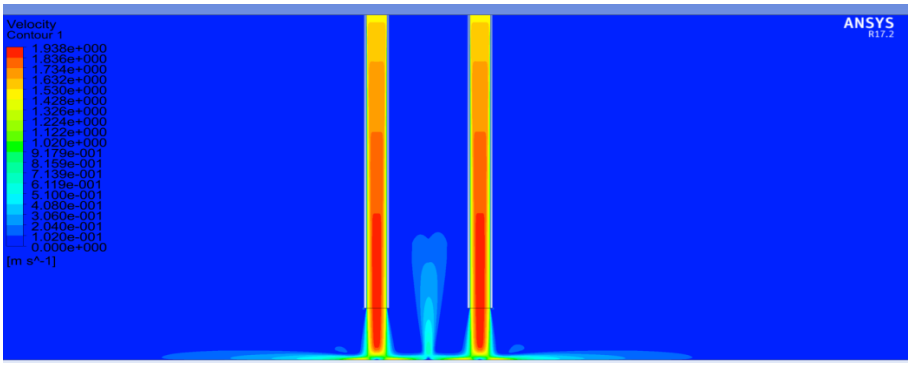

Figure 2.6 Fountain formed by two identical jets

2.3.2 Straight Up-Wash Fountain

Figure 2.7 shows the velocity streamlines in a fountain formed by two jets where S/D = 16, H/D = 3 and V1 = V2 = 2.5m/s. In the region away from the bottom plane, two upstream vortices are formed on two sides of the fountain as shown in Figure 2.7(a). In the region close to bottom plane, two ground vortices are formed on two sides of the fountain as shown in Figure 2.7 (b). Although an up-wash fountain is formed in the middle of two jets, the flow is down-wash in the region very close to ground.

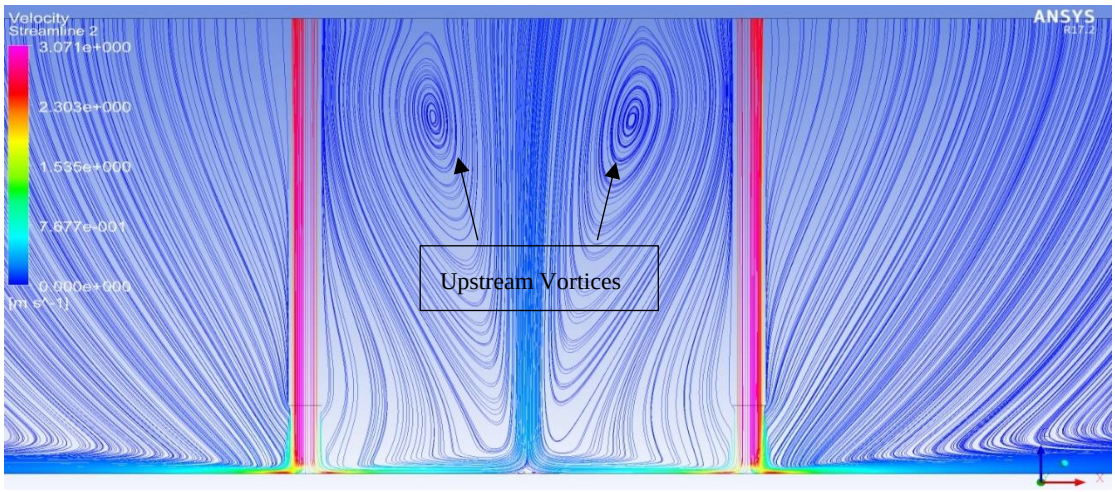

(a) Up-stream vortices on two sides of fountain

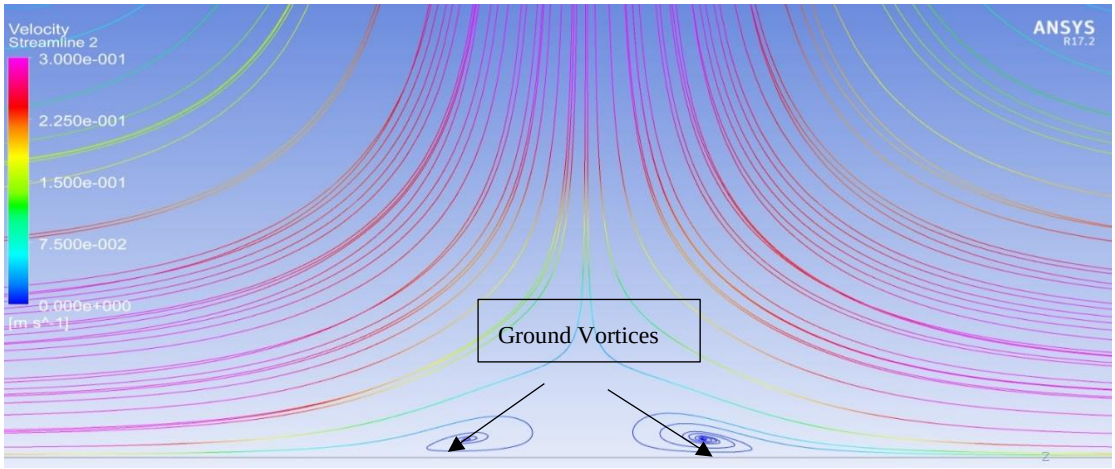

(b) Vortices near ground on two sides of the fountain

Figure 2.7 Velocity streamlines in a fountain formed by two jets.

For the same simulation, Figure 2.8(a) and Figure 2.8(b) show the velocity distribution at different radial distances from the centerline of the fountain, ranging from 0D to 4D. The velocity distributions show different characteristics before and after x/D = 0.5. Velocity increases at smaller rate when x/D is less than 0.5 compared to when it is larger than 0.5. Peak velocity decreases as x/D increases when x/D is less than 0.5; on the other hand if x/D is larger than 0.5, peak velocity increases as x/D becomes larger.

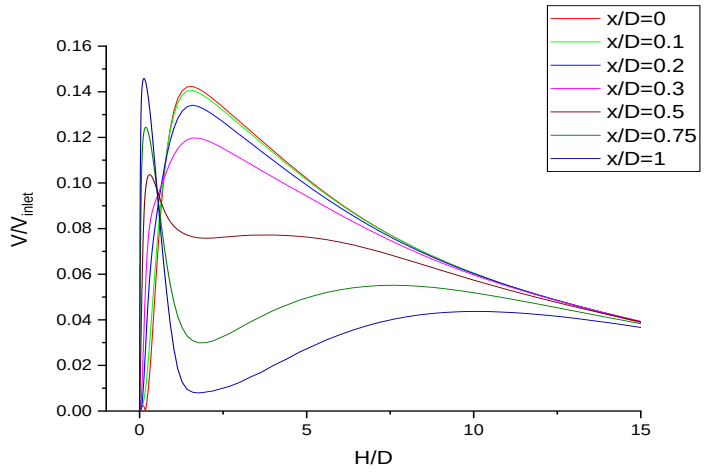

(a) when 0 < x/D <1

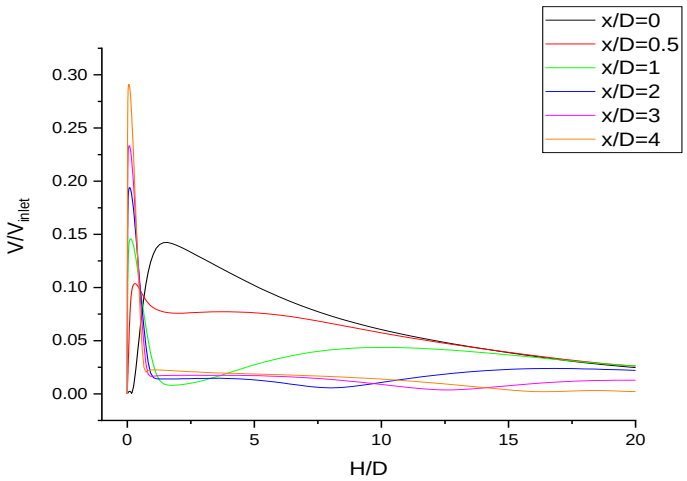

(b) when 0 < x/D <4

Figure 2.8 Normalized vertical velocity distribution for various radial distances, x/D.

Figures 2.9(a) and 2.9 (b) show the location and magnitude of maximum velocity respectively at different radial distances from the centerline of the fountain; they are normalized by the diameter of the jet and inlet velocity respectively. Fountain shows different flow characteristics when x/D < 0.5 and when x/D > 0.5. Maximum velocity occurs significantly close to ground when x/D > 0.5. Maximum velocity increases gradually as x/D gets larger than 0.5.

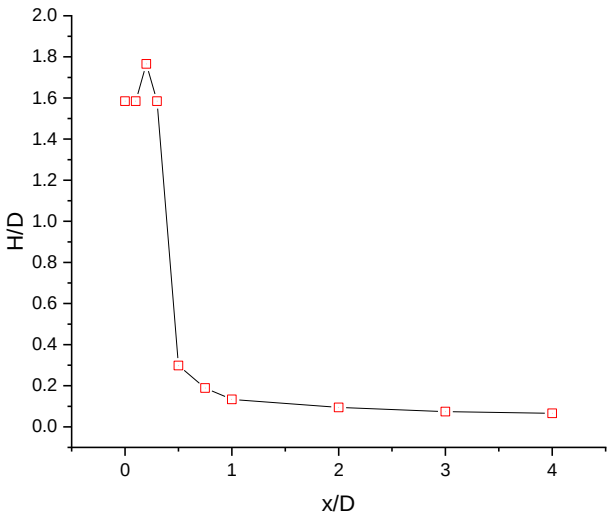

(a): Location of maximum velocity

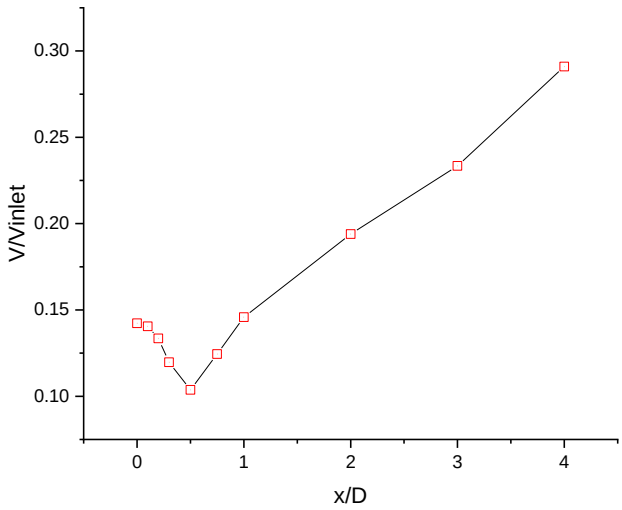

Figure 2.9 (b): Normalized maximum velocity

Figure 2.9 Location and magnitude of maximum velocity at various radial distances, x/D

2.3.3 Straight Fountain Formation under Various Flow Conditions

A series of simulations is performed when Reynolds numbers at two velocity inlets of the two jets are the same. Diameters of the two jets are set identical at 0.02m. Inlet velocity is set at 1m/s, 1.5m/s, 2m/s and 2.5m/s, and corresponding Reynolds numbers are 20,000, 29,900, 39,900 and 49,900 respectively. Figure 2.10 shows the logarithm of stagnation pressure coefficient, defined as $C_p = \frac{P-\rho gh}{0.5\rho v_{inlet}^2}$, versus logarithm of inlet Reynolds number at different conditions when parameters including the distance between twin jets, S/D and impingement height H/D are changed. For fixed S/D, logarithm of pressure coefficient and logarithm of inlet Reynolds number show linear relationship. Furthermore, change in impingent height leads to greater change in pressure coefficient for small S/D, such as 1.4, while pressure coefficient for S/D=16 changes slightly.

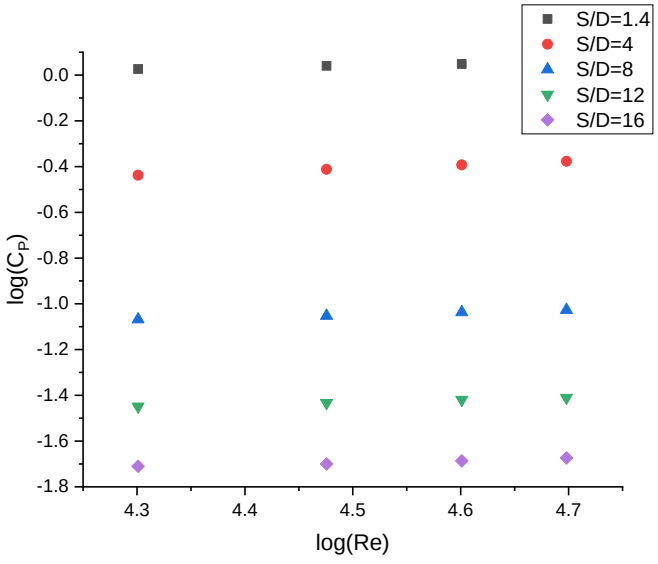

(a) Impingement height = 3D

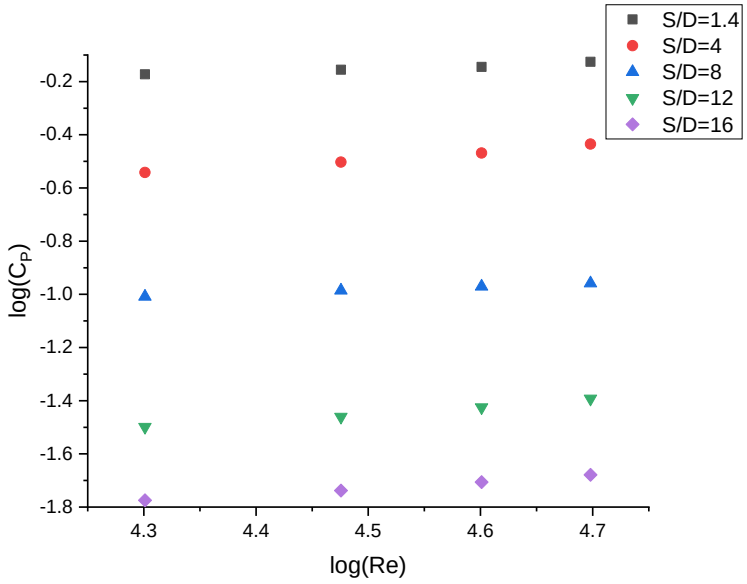

(b) Impingement height = 6D

Figure 2.10 Variation in pressure coefficient at stagnation point of the fountain with inlet Reynolds number for various cases.

Figure 2.11 and Figure 2.12 show the location and magnitude of maximum velocity at centerline of fountain under various conditions. For fixed twin-jet distance and impingement height, location of maximum velocity at centerline of the fountain does not change with inlet Reynolds number. Maximum velocities for S/D = 1.4 and 4 at centerline are very close especially when impingement height is 3D. And change in impingement height has greater influence on maximum velocity of the centerline for S/D = 1.4 and 4 than on that for S/D = 8, 12 and 16. Larger the S/D value is, less is the influence of change in impingement height on maximum velocity of the centerline of the fountain.

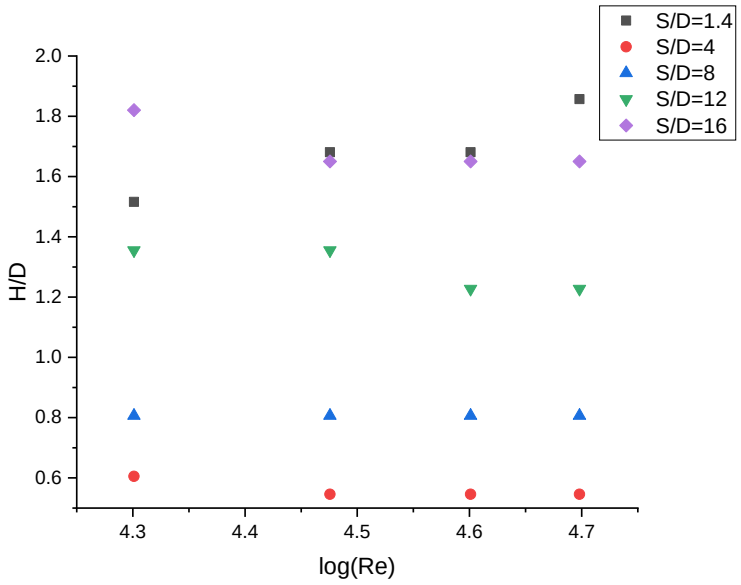

(a) Impingement height = 3D

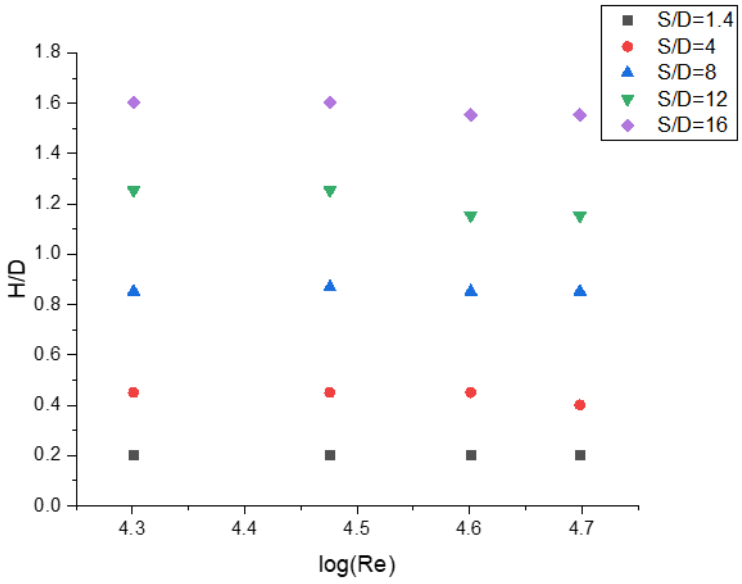

(b) Impingement height = 6D

Figure 2.11 Location of maximum velocity at centerline of the fountain for various conditions.

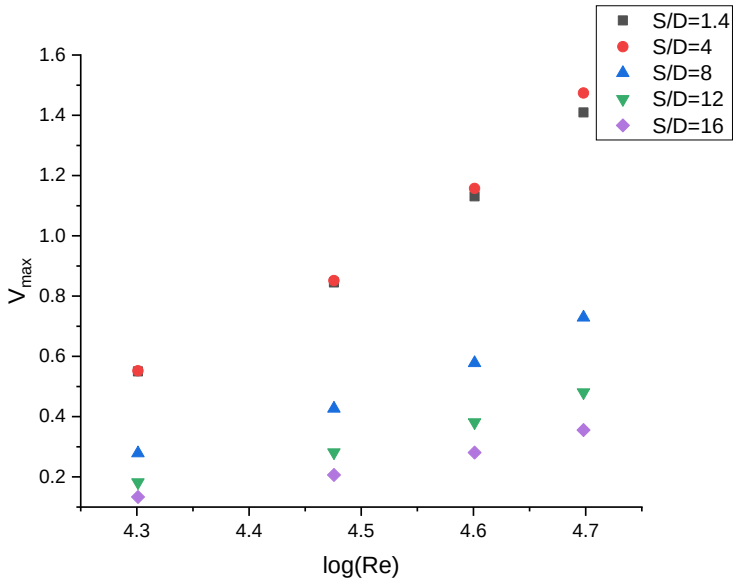

(a) Impingement height =3D

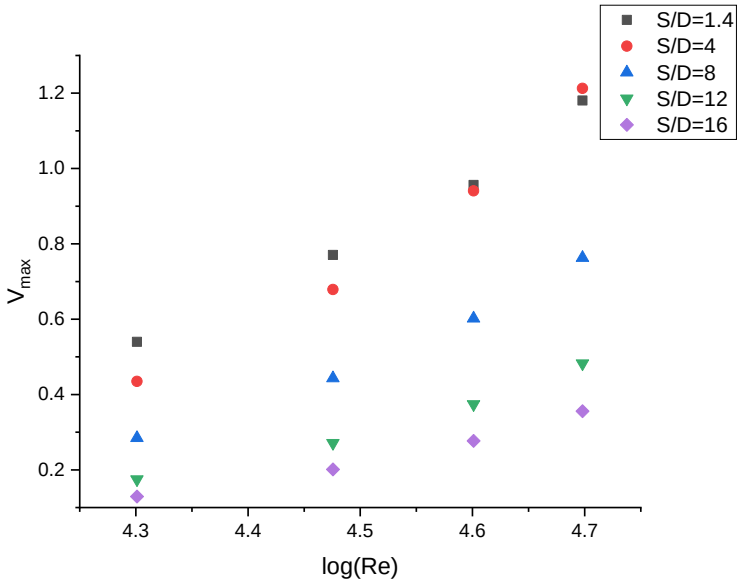

(b) Impingement height = 6D

Figure 2.12 Magnitude of maximum velocity at centerline of fountain at various conditions.

2.3.4 Inclined Fountain Formation

Differences in Reynolds numbers of the two jets lead to formation of fountain that moves and curves towards the jet with smaller Reynolds number. In this case, character of the fountain is highly influenced by the ratio of the Reynolds numbers at jet inlets. Inlet velocity of right jet is changed to achieve different ratio of Reynolds numbers, while inlet velocity of left jet is fixed at 1m/s ($Re = 2*10^4$). Distance between the two jets is fixed at 5D. Figures 13~21 show velocity contours of inclined fountain for various ratio of Reynolds numbers, for velocities between 0 and 1m/s. By connecting upper and lower boundary of velocity contour, the formed lines display similar velocity distribution as centerline of straight fountain. Therefore, these lines can be treated as centerlines of inclined fountain. Location and velocity distribution of centerline of inclined fountain are also included in Figures 14~18. When the ratio of Reynolds numbers becomes larger than 3.3, it becomes very hard to identify the centerline of the inclined fountain. As the ratio of Reynolds numbers increases, stagnation point of the fountain moves towards the left jet that has smaller Reynolds number than the right jet. As ratio of Reynolds number reaches 3.8, the stagnation point of fountain almost overlaps with that of the left jet impingement. Furthermore, fountain is also inclined to the same side. However, when ratio of Reynolds numbers is larger than 2.5, as can be observed in Figure 2.17, fountain reflects from the left jet and moves back towards the right jet.

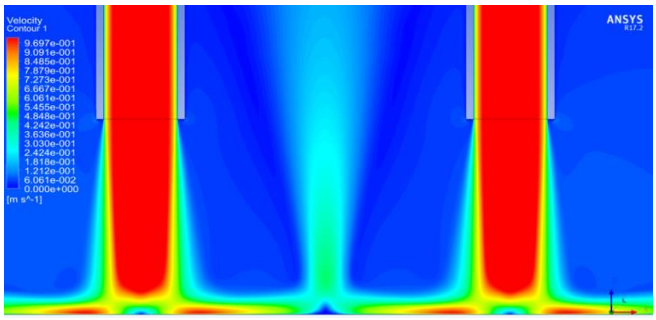

Figure 2.13 Straight Fountain when R_{Re} =1

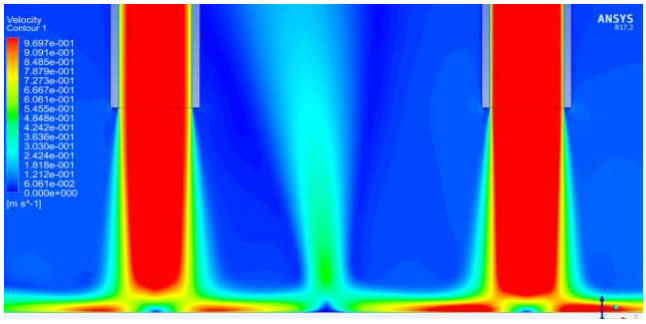

(a) Velocity contours

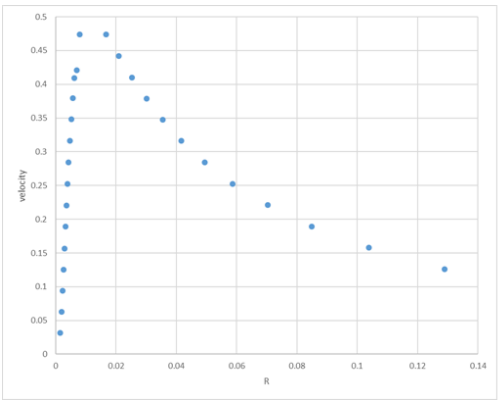

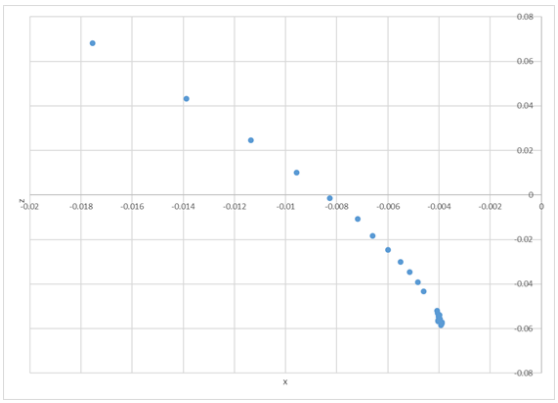

(b) Velocity distribution and location of centerline of the fountain.

Figure 2.14 Inclined fountain when R_{Re} =1.2

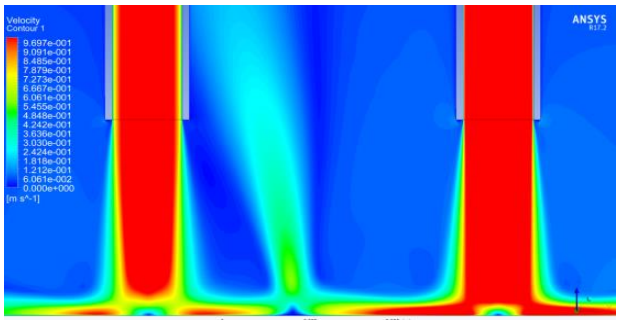

(a) Velocity contours

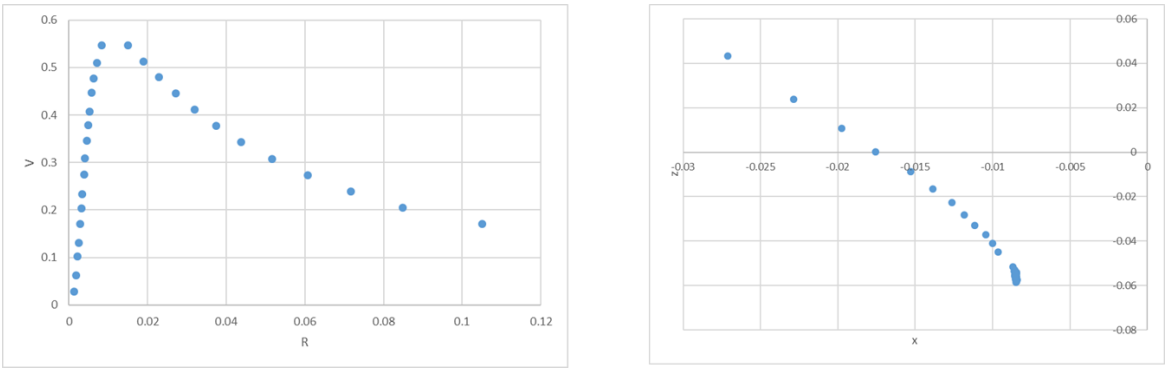

(b) Velocity distribution and location of centerline of the fountain.

Figure 2.15 Inclined fountain when R_{Re} =1.5.

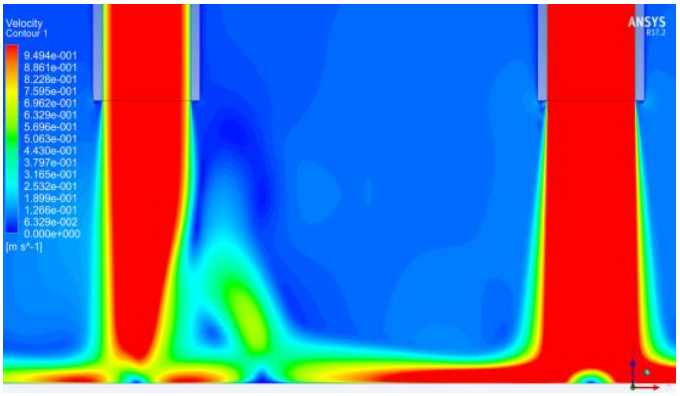

(a) Velocity contours

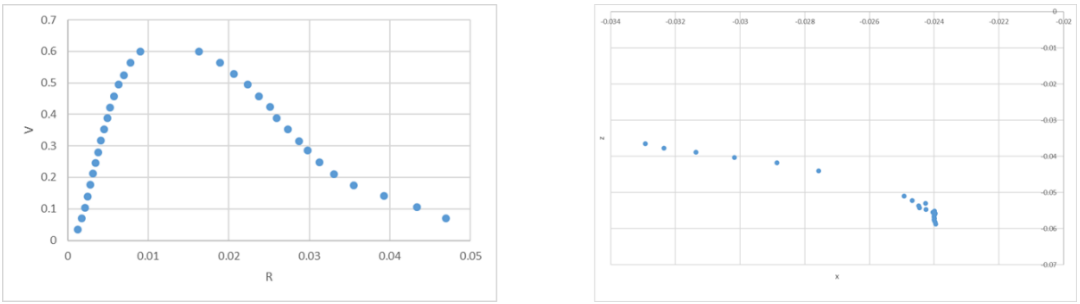

(b) Velocity distribution and location of centerline of the fountain.

Figure 2.16 Inclined fountain when R_{Re} =2.

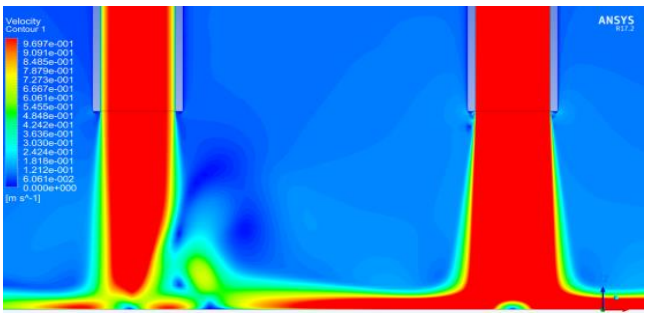

(a) Velocity contours

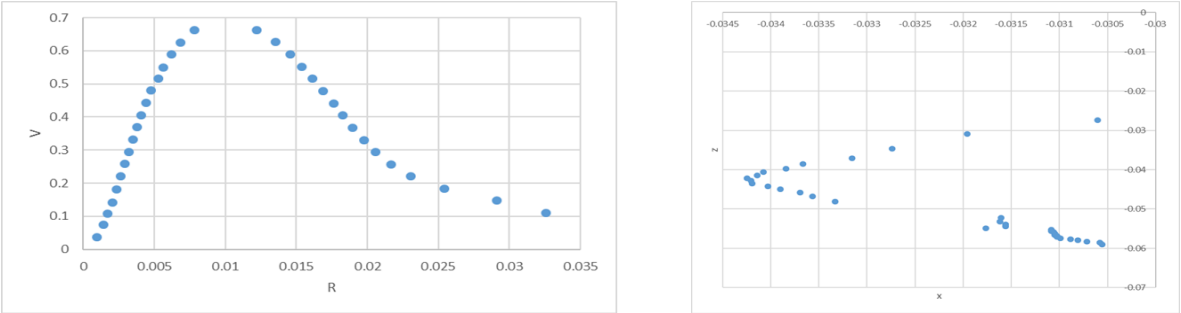

(b) Velocity distribution and location of centerline of the fountain.

Figure 2.17 Inclined fountain when R_{Re} =2.5.

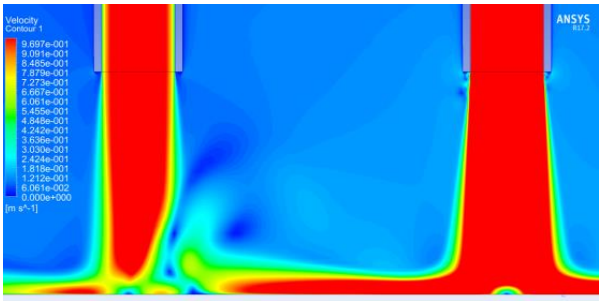

(a) Velocity contours

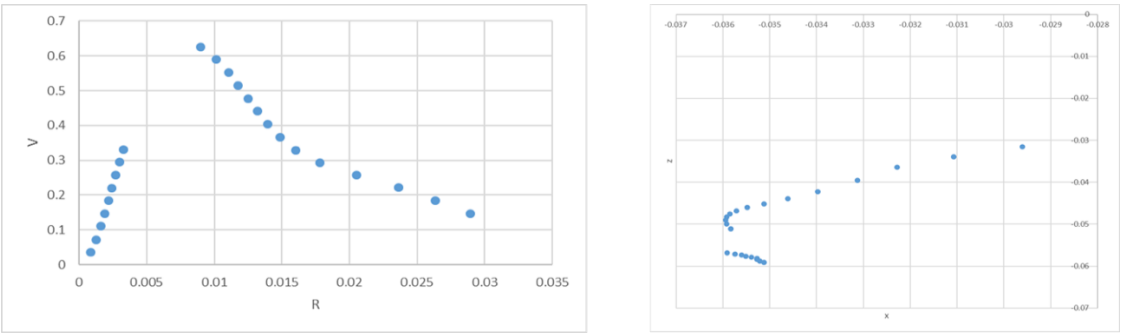

(b) Velocity distribution and location of centerline of the fountain.

Figure 2.18 Inclined fountain when R_{Re} =3.

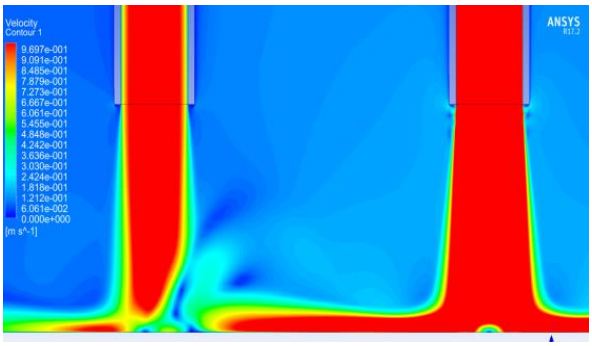

Figure 2.19 Inclined fountain when R_{Re} =3.3.

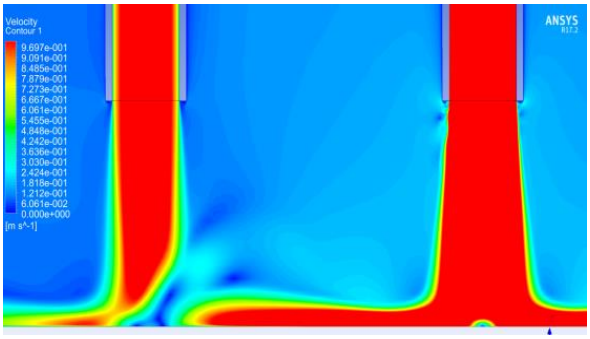

Figure 2.20 Inclined fountain when R_{Re} =3.8.

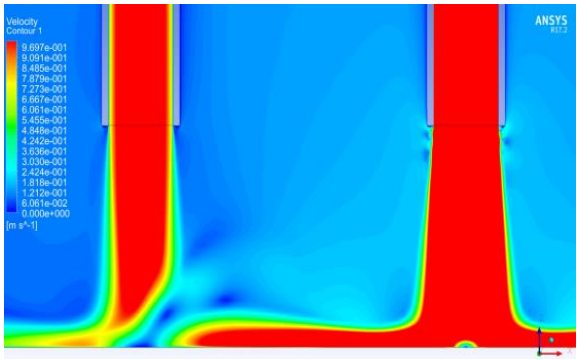

Figure 2.21 Inclined fountain when R_{Re} =4.

Pressure distribution at the bottom plane when R_{Re} is 3.3 is shown in Figure 2.22 (a). Two peak values in the pressure can be seen; the left one corresponds to the stagnation point of the left jet while the right one is the stagnation point of the formed fountain. However, for cases where R_{Re} is 3.8 and 4, the second peak cannot be observed as distinctly as shown in Figure 2.22 (b) and Figure 2.22 (c).

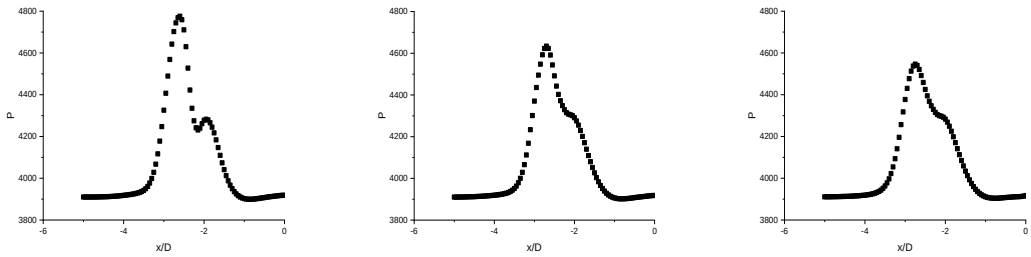

(a) R_{Re} =3.3 (b) R_{Re} =3.8 (c) R_{Re} =4

Figure 2.22 Pressure distribution in the bottom plane under different R_{Re}

Figure 2.23 shows the location of stagnation point of the fountain normalized by diameter of jet for various ratios of Reynolds number. When R_{Re} is 1, fountain is straight upward and stagnation point is at x/D = 0, right in the middle of the two jets as expected. As R_{Re} increases, stagnation point of the fountain approaches x/D = -2.5 which is the centerline of the left jet. And for R_{Re} > 3.3, the movement of stagnation point decreases greatly. Figure 2.24 shows the static pressure at stagnation points. Similarly, before R_{Re} reaches 3.3, pressure at stagnation point increases more rapidly compared to that when R_{Re} increases beyond 3.3 when it changes more slowly and pressure at stagnation point approaches 4300Pa where 3916Pa is generated by water due to gravity acceleration.

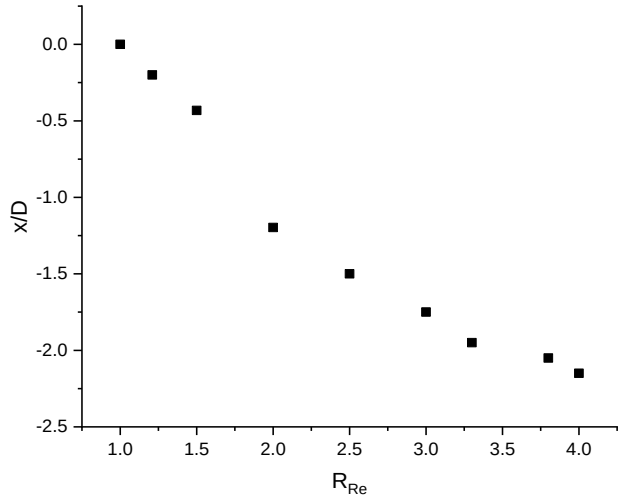

Figure 2.23 Variation in location of stagnation point of the fountain for various R_{Re}.

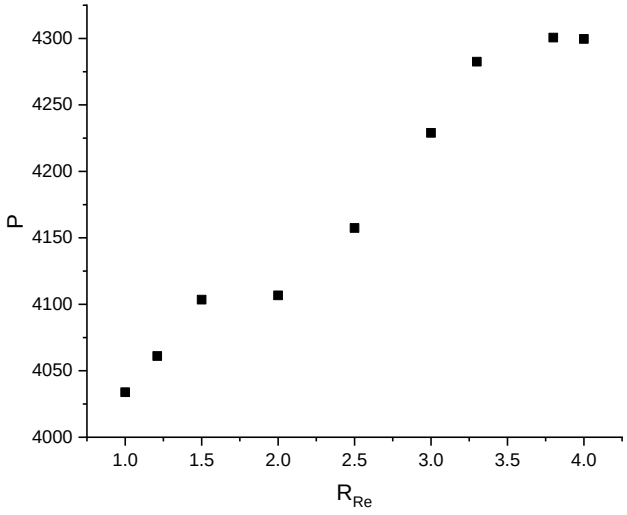

Figure 2.24 Variation in static pressure at stagnation point of fountain with R_{Re}.

Figure 2.25 shows the displacement of stagnation point of left jet for different values of R_{Re}. Displacement of stagnation point of left jet for $R_{Re} > 3.3$ is much faster than for $R_{Re} < 3.3$. Figure 2.26 shows the static pressure at stagnation point. Similarly, for $R_{Re} > 3.3$, the pressure at stagnation point of left jet decreases significantly. This phenomenon could be the result of strong wall jet produced by right jet when $R_{Re} > 3.3$. Vertical velocity component of wall jet from right side prevents left jet from

impinging on the bottom plate. Therefore, decayed impingent of left jet reduces pressure at stagnation point of left jet.

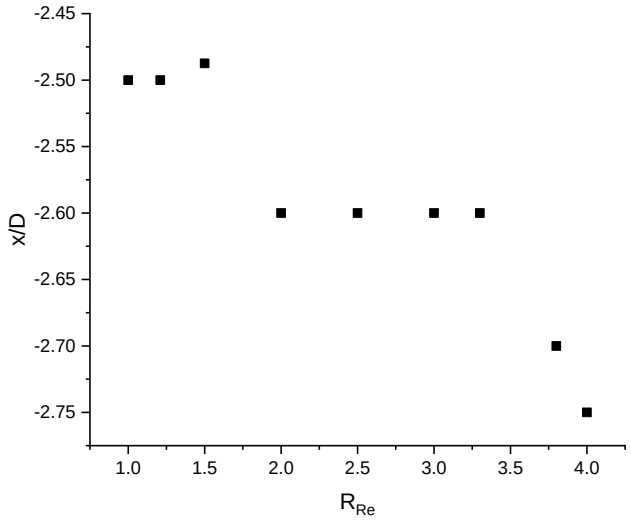

Figure 2.25 Variation in location of stagnation point of left jet with R_{Re}.

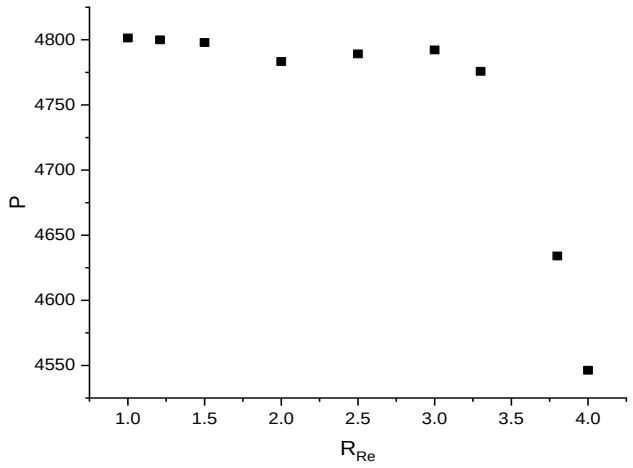

Figure 2.26 Variation in pressure at stagnation point of left jet with R_{Re}.

2.4 Conclusions

Based on the results presented in this section, the following conclusions can be drawn:

1) For fountain formed by two round jets, if Reynolds number of the two jets at inlet

is identical and exits of jets are located at same horizontal level, the fountain formed in this condition will be straight and upwards.

2) Pressure at fountain center is highly sensitive to the inlet Reynolds number of the jets when distance between the jets, S, is small. However, pressure coefficient is much less sensitive to inlet Reynolds number than pressure in Pascal.

3). Straight fountain exhibits different velocity profiles in regions at different radial distances. Fountain flow has larger acceleration in the bottom plane when radial distance, x/D, is more than 0.5 than it has when x/D is less than 0.5.

4). When inlet Reynolds number of jets are different, fountain formed by the two jets moves to the side of the jet with smaller inlet Reynolds number and stagnation point of the fountain also moves along in the same direction. As ratio of Reynolds number increases, fountain reflects back from the jet with larger inlet Reynolds number and stagnation point of the fountain tends to merge with stagnation point of the left jet that has smaller inlet Reynolds number. Meanwhile, strong wall jet from right side has a negative influence on impingement of left jet.

References

[1] Weigand, B., & Spring, S. (2011). Multiple jet impingement− a review. Heat Transfer Research, 42(2).

[2] Jambunathan, K., Lai, E., Moss, M. A., & Button, B. L. (1992). A review of heat transfer data for single circular jet impingement. International journal of heat and fluid flow, 13(2), 106-115.

[3] Adane, K. F. K., & Tachie, M. F. (2010). Experimental and numerical study of laminar round jet flows along a wall. Journal of Fluids Engineering, 132(10), 101203.

[4] Dewan, A., Dutta, R., & Srinivasan, B. (2012). Recent trends in computation of turbulent jet impingement heat transfer. Heat Transfer Engineering, 33(4-5), 447-460.

[5] Wang, C., Wang, X., Shi, W., Lu, W., Tan, S. K., & Zhou, L. (2017). Experimental investigation on impingement of a submerged circular water jet at varying impinging angles and Reynolds numbers. Experimental Thermal and Fluid Science, 89, 189-198.

[6] Ghaneeizad, S. M., Atkinson, J. F., & Bennett, S. J. (2015). Effect of flow confinement on the hydrodynamics of circular impinging jets: implications for erosion assessment. Environmental Fluid Mechanics, 15(1), 1-25.

[7] Shademan, M., Balachandar, R., & Barron, R. M. (2013). CFD analysis of the effect of nozzle stand-off distance on turbulent impinging jets. Canadian Journal of Civil Engineering, 40(7), 603-612.

[8] Greco, C. S., Ianiro, A., Astarita, T., & Cardone, G. (2013). On the near field of single and twin circular synthetic air jets. International Journal of Heat and Fluid Flow, 44, 41-52.

[10] Ostheimer, D., & Yang, Z. (2012). A CFD study of twin impinging jets in a cross-flow.

[11] Saripalli, K. R. (1983). Visualization of multijet impingement flow. AIAA Journal, 21(4), 483-484.

[121] Ozmen, Y. (2011). Confined impinging twin air jets at high Reynolds numbers. Experimental Thermal and Fluid Science, 35(2), 355-363.

[13] Barata, J. M., Durao, D. F. G., Heitor, M. V., & McGuirk, J. (1991). Impingement of single and twin turbulent jets through a crossflow. AIAA journal, 29(4), 595-602.

[14] Abdel-Fattah, A. (2007). Numerical and experimental study of turbulent impinging twin-jet flow. Experimental Thermal and Fluid Science, 31(8), 1061-1072.

Curriculum Vita

Xiang Zhang

Degrees

M.S. in Mechanical Engineering, Washington University in St. Louis, Missouri, May 2019

B.S. in Aircraft Propulsion Engineering, Civil Aviation University of China, Tianjin, China, July 2017